Despeckling Multitemporal Polarimetric SAR Data Based on Tensor Decomposition

Jiayin Luo , Lu Zhang , Jie Dong , Juan M. Lopez-Sanchez , *Senior Member, IEEE*, Yian Wang , Hao Feng , and Mingsheng Liao

Abstract—Despeckling is an essential task in polarimetric synthetic aperture radar (PolSAR) image processing. Most of the existing filters developed for multitemporal synthetic aperture radar (SAR) images make use of either real or complex information. Real information refers to amplitude or intensity values, whereas complex information refers to complex covariance matrix (CCM) derived from either interferometric SAR (InSAR) or PolSAR data. The InSAR CCM is formed using images of the same polarimetric channel but acquired at different dates, and the PolSAR CCM contains information acquired simultaneously in different polarimetric channels. Therefore, these despeckling methods may present good performance in some applications and scenes but fail in other cases, due to differences in input sources. In order to achieve a more robust result in all cases, we develop a method for multitemporal polarimetric SAR data filtering based on tensor decomposition, which aims at improving the identification of homogeneous pixels for spatially adaptive filtering. The key element of this approach consists of exploiting tensor theory to construct a new CCM that contains both polarimetric and interferometric information, as well as multitemporal information for each pixel. The effectiveness of the proposed method and its performance are evaluated with simulated and real SAR data in comparison with several established methods.

I. INTRODUCTION

MODERN synthetic aperture radar (SAR) systems provide an unprecedented ability to acquire polarimetric images over the same area with high revisit frequency. Polarimetric SAR (PolSAR) is an advancement over the conventional single-polarization SAR because of the additional information content of the various polarimetric channels measured. Polarization diversity enhances discrimination capabilities, which can benefit in, for example, forest, agriculture, cryosphere, urban, and ocean applications [1]. Unfortunately, SAR images are intrinsically contaminated by speckle, which complicates the aforementioned applications.

In the past decades, single-polarization SAR images have been vastly used for applications such as ground surface deformation monitoring [2], [3], [4] and land cover mapping [5]. As a result, speckle filters are mainly focused on intensity or interferometric complex information. The simplest despeckling method is the spatial multilooking process, which consists in averaging neighbor pixels within a spatial window. If the window is predefined, e.g., rectangular, it achieves good smoothing at the cost of blurring spatial details and fine structures. To avoid selecting pixels that belong to different targets, adaptive techniques were proposed. Since 1980s, filters based on the minimum mean square error (MMSE) [6], [7] have been widely applied, as they consider local statistics. Several improved algorithms have been derived from MMSE filters, such as Kuan [8], Frost [9], and the recently improved iterative MMSE filter [10] (and its PolSAR version [11]). Later, the intensity-driven adaptive-neighborhood filter [12] was proposed, which requires good connectivity between pixels. Based on the concept of patch matching, single-temporal SAR filtering methods, such as probabilistic patch-based method [13], SAR block matching 3-D method [14], weighted sparse representation despeckle method [15], and also multitemporal SAR block-matching 3-D (MSAR-BM3D) method [16], lead to a good performance, especially in detail preservation. Innovative methods based on multichannel logarithm with Gaussian denoising were proposed in [17], [18], and [19], and deep learning methods were also adapted to SAR speckle filtering [20], [21], [22]. To reduce speckle in multitemporal sets of images more efficiently, some fast strategies were introduced in [23].

Another hot topic in this domain is the use of adaptive filters based on identifying statistically homogeneous pixels (SHPs) through a region growing method, which exploits the similarity of backscatter intensity [24], [25], [26], [27], [28]. In the context of differential interferometry (DInSAR) based on time series, the DespecKS method was designed for the $SqueeSAR^{TM}$ technique [24]. Similarity between a central pixel and its surroundings is estimated by the Kolmogorov–Smirnov test [29]. To overcome the computational burden of DespecKS, the fast SHP selection (FaSHPs) [25] and its variant [30] were developed. They construct a confidence interval for each pixel using the amplitude images and select SHPs according to that interval. However, all the methods mentioned here only consider the real values of the images (amplitude or intensity). In order to exploit interferometric complex information, the complex-covariance-matrix-based multitemporal filter (CCM-MTF) [26] and the covariance matrix patch filter [31] were proposed. They identify SHPs by using the generalized likelihood ratio test [32] to compare InSAR CCMs of the reference pixel and its surrounding pixels.

Recently, satellites with extended polarimetric capabilities, such as Radarsat-2, TerraSAR-X, ALOS PALSAR, and Sentinel-1, have enabled the access to multitemporal PolSAR images. As PolSAR data are sensitive to physical characteristics of the scene, despeckling filters based on PolSAR information were developed. Examples include the refined Lee filter [33], the model-based PolSAR filters [34], [35], and the total-variation-based methods [36], [37], [38]. Recently, PolSAR filters based on binary partition trees (BPTs) [39], [40], deep learning [41], infinite number of looks prediction [42], and nonlocal strategy [19], [43], [44] were proposed.

Most of these algorithms were developed for PolSAR data or InSAR data acquired at a single date or two dates at most. In addition, a ratio-based speckle reduction approach for multitemporal PolSAR images was introduced in [45]. Moreover, the GLR test on the averaged PolSAR CCM was exploited in a multitemporal polarimetric filter (MPF) [28] for the extension of differential interferometry with PolSAR data.

In general, available filters based on complex information only use the InSAR CCM and ignore the PolSAR CCM, or *vice versa*. To the best of the authors' knowledge, limited research exists on using interferometric and polarimetric information jointly for despeckling. One study uses the sum of Kronecker product decomposition to extract polarimetric and interferometric coherence information simultaneously [46], but it is only applicable to fully polarimetric data. The most recent study exploiting both interferometric and polarimetric information is based on BPTs [40].

In order to utilize the multitemporal InSAR and PolSAR information in a simple and efficient way, in this article, we propose a novel tensor-decomposition-based multitemporal polarimetric filter (TD-MPF). The key aspect of this filter is the generation of a new CCM, which jointly contains the information of the InSAR CCM and the PolSAR CCM for the given multichannel images. This new CCM is constructed using tensor formulation. The reason for employing tensors is that they can jointly process multi-dimensional information (spatial, spectral, and temporal) [47], [48], [49], [50]. Once the tensor-based CCM is constructed for every pixel, the set of SHPs of each pixel can be identified by applying the GLR test between their CCMs, and finally, the estimated CCM is computed by averaging over the SHPs.

Both simulated and real PolSAR datasets acquired for a short period are used to verify the effectiveness of the proposed method. The filtering results are compared against MSAR-BM3D, FaSHPS, CCM-MTF, and MPF. These methods were chosen because their strategies are different and their codes are available.

II. METHODOLOGY

Throughout this article, scalars are denoted by italic lowercase and uppercase letters (e.g., m and N), vectors are denoted by boldface lowercase letters (e.g., $\mathbf{k}$), matrices are represented by bold uppercase letters (e.g., $\mathbf{C}$ and $\mathbf{U}$), and tensors are denoted by calligraphy letters (e.g., $\mathcal{X}$, $\mathcal{Y}$, and $\mathcal{C}$). The overall processing flow is shown in Fig. 1, in which p indicates the number of images used and m is the number of polarization channels.

A. Statistical Descriptors of Multitemporal Data

1) Quad-Pol Data: To construct a tensor that contains the information of multitemporal quad-pol data, it is necessary to obtain two types of covariance matrix: a polarimetric covariance matrix and a single-polarization interferometric covariance matrix for each polarimetric channel.

For each pixel, a single-look complex PolSAR image acquired at date t_a is represented by a scattering vector $\mathbf{k}_{\text{FP},t_a}$, which is formed under the assumption of reciprocity as follows:

$$\mathbf{k}_{\text{FP},t_a} = [S_{\text{HH},t_a}, S_{\text{HV},t_a}, S_{\text{VV},t_a}]^T \quad (1)$$

where the superscript T denotes the matrix transpose operator, FP indicates fully polarimetric, and S_{HV,t_a} is the complex backscattering coefficient measured by transmitting horizontal polarization and receiving vertical polarization, acquired at time t_a. The other elements are defined similarly.

The multilook of the polarimetric CCM is performed over samples at the same position along the temporal dimension. For p-dimensional temporal images, i.e., when there are p acquisition times, the PolSAR CCM can be obtained as

$$\mathbf{C}_{\text{FP}} = \frac{1}{p} \sum_{t_a=1}^{p} \mathbf{k}_{\text{FP},t_a} \mathbf{k}_{\text{FP},t_a}^{H} \quad (2)$$

where H denotes transpose and conjugation. The size of the resultant matrix is 3×3.

The formation of the interferometric CCM is inspired by the CCM-MTF method [26]. A single polarization scattering vector of dimension p, denoted as $\mathbf{k}_{\text{SP}}$ (where SP represents the single polarimetric channel, e.g., $\mathbf{k}_{\text{VV}}$, $\mathbf{k}_{\text{HH}}$, $\mathbf{k}_{\text{HV}}$, or $\mathbf{k}_{\text{VH}}$), can be grouped into p/m scattering vectors $\mathbf{k}'_{\text{SP}}$ of m-dimension. For quad-pol data, we set $m = 3$; hence

$$\mathbf{k}_{\text{SP}} = [S_{\text{SP},t_1}, S_{\text{SP},t_2}, \dots, S_{\text{SP},t_{p-1}}, S_{\text{SP},t_p}] \quad (3)$$

$$\mathbf{k}'_{\text{SP},t_b} = [S_{\text{SP},t_a}, S_{\text{SP},t_{a+1}}, S_{\text{SP},t_{a+2}}]^T$$
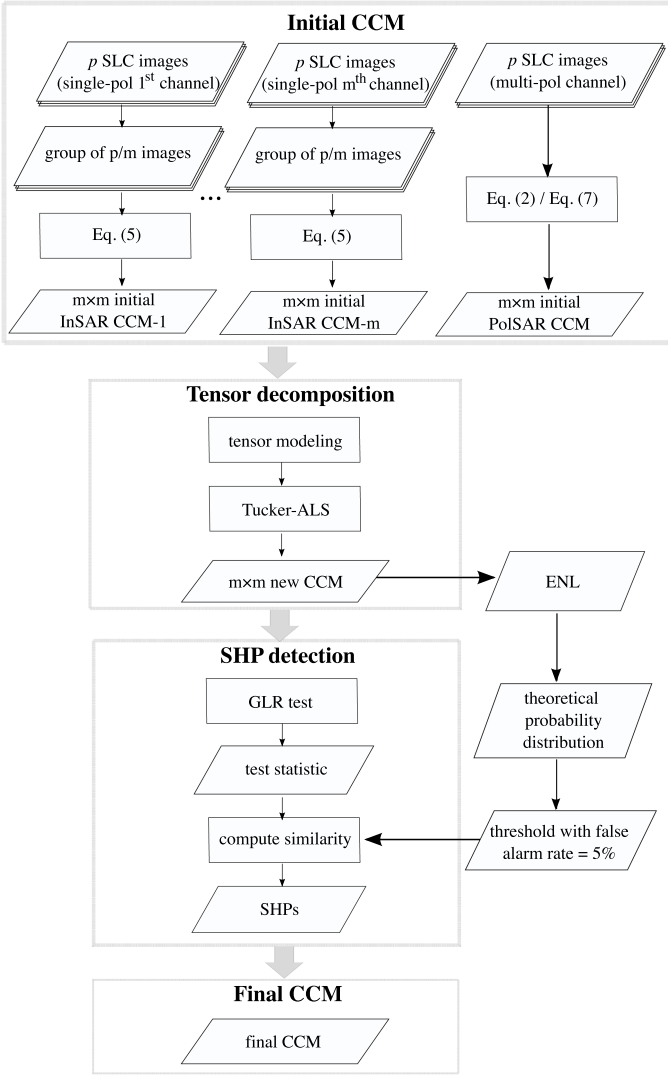$$b = 1, 2, \dots, p/3; a = 3b - 2. \quad (4)$$

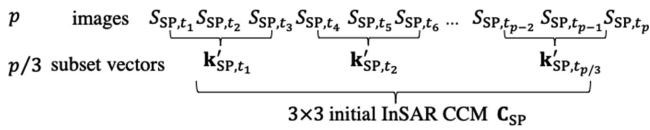Fig. 1. Flowchart of the main steps performed by the proposed tensor-based method.

Fig. 2. Procedure to estimate the initial InSAR CCM for the quad-pol case.

Each single-polarization interferometric CCM, i.e., $\mathbf{C}_{VV}$, $\mathbf{C}_{HH}$, $\mathbf{C}_{HV}$, or $\mathbf{C}_{VH}$ of size 3×3, can be computed as

$$\mathbf{C}_{SP} = \frac{1}{p/3} \sum_{t_b=1}^{p/3} \mathbf{k}'_{SP,t_b} \mathbf{k}'_{SP,t_b}{}^H. \qquad (5)$$

The procedure to estimate $\mathbf{C}_{SP}$ for each channel in the quad-pol case is illustrated in Fig. 2. The combination of images into $p/3$ scattering vectors is motivated by the goal of forming polarimetric and interferometric matrices of equal dimensions, so that they can be later stacked as a tensor.
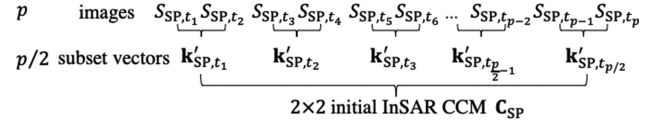

Fig. 3. Procedure to estimate the initial InSAR CCM for the dual-pol case.

2) Dual-Pol Data: The much wider availability of dual-pol data, compared to quad-pol data, from satellites such as Sentinel-1 makes it a suitable option for testing the performance of the proposed method.

For dual-pol data with VV and VH channels (which can also be altered to include other polarization channels, i.e., HH and VV, or HH and HV), the scattering vector at one pixel becomes

$$\mathbf{k}_{DP,t_a} = [S_{VV,t_a}, S_{VH,t_a}]^T. \qquad (6)$$

Then, the multilook of the polarimetric CCM of size 2×2 is defined as

$$\mathbf{C}_{DP} = \frac{1}{p} \sum_{t_a=1}^{p} \mathbf{k}_{DP,t_a} \mathbf{k}_{DP,t_a}{}^H. \qquad (7)$$

As there are only two channels in dual-pol data, only two interferometric CCM can participate in the construction of the tensor, for example, $\mathbf{C}_{VV}$ and $\mathbf{C}_{VH}$. To obtain these matrices, it is also necessary to group the available p-dimensional temporal images in (3) into p/m scattering vectors of m-dimension, where m equals 2 for dual-pol data:

$$\mathbf{k}'_{SP,t_b} = [S_{SP,t_a}, S_{SP,t_{a+1}}]^T$$
$$b = 1, 2, \ldots, p/2; a = 2b - 1. \qquad (8)$$

The procedure to estimate $\mathbf{C}_{SP}$ for each channel in the dual-pol case is illustrated in Fig. 3.

Finally, the single-polarization interferometric matrix of each channel, with size 2×2, is computed according to (9).

$$\mathbf{C}_{SP} = \frac{1}{p/2} \sum_{t_b=1}^{p/2} \mathbf{k}'_{SP,t_b} \mathbf{k}'_{SP,t_b}{}^H. \qquad (9)$$

B. Tensor Modeling of Multitemporal PolSAR Images

According to the assumption of reciprocity and using (2), (5), and (7), a total of four ($\mathbf{C}_{FP}$, $\mathbf{C}_{HH}$, $\mathbf{C}_{VV}$, $\mathbf{C}_{HV}$) and three covariance matrices ($\mathbf{C}_{DP}$, $\mathbf{C}_{VV}$, $\mathbf{C}_{VH}$) (for our datasets) are collected to provide a comprehensive description of one pixel with quad-pol and dual-pol multitemporal data, respectively. The detail of the construction of the tensor is illustrated in Fig. 4 for quad-pol data and for two combinations of dual-pol data (HH and VV, VV and VH).

It is important to note that, if prior knowledge of the scene is available, the weights assigned to the polarimetric and interferometric matrices can be adjusted to obtain specific results. In this study, equal weights are set for the PolSAR CCM and the InSAR CCM. According to the notation in Fig. 4, this means that $w_1 = 0.5$, and $w_2 + w_3 + w_4 = 0.5$ or $w_2 + w_3 = 0.5$, with $w_2 = w_3 = w_4$.
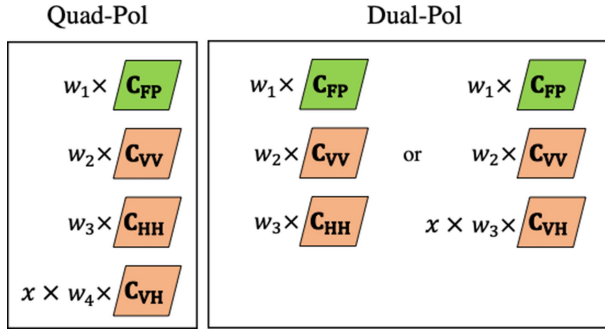
Fig. 4.   Scheme of the composition of tensors for one pixel and their associated weights. Left: quad-pol case. Right: dual-pol case with two different combinations of channels.

Since the intensity of the cross-polar channel (VH or HV) is significantly lower than that of the copolar channels (HH and VV), it is essential to compensate its weight before proceeding with the tensor modeling. For this purpose, parameter x is employed for $\mathbf{C}_{VH}$ (see Fig. 4), obtained as the maximum ratio between the median intensity value of the VV (or HH) channel and the VH channel for all acquisition dates, i.e.,

$$x = \max\left(\frac{\text{median}(\mathbf{INT}_{VV,t_a})}{\text{median}(\mathbf{INT}_{VH,t_a})}, \frac{\text{median}(\mathbf{INT}_{HH,t_a})}{\text{median}(\mathbf{INT}_{VH,t_a})}\right)$$
$$a = 1, 2, \ldots, p \tag{10}$$

where $\mathbf{INT}_{VV,t_a}$ is the intensity value of the VH channel at acquisition time t_a, and similar definitions apply for the other parameters. In case of using only the copolar channels, VV and HH, the calculation of x is not required.

At this stage, these matrices can be combined to create a five-order tensor $\mathcal{X} \in \mathbb{R}^{F_1 \times F_2 \times F_3 \times F_4 \times F_5}$, where F_1 and F_2 indicate the spatial dimensions of the image, $F_3 = F_4 = m$, and $F_5 = 4$ for quad-pol data or $F_5 = 3$ for dual-pol data, reflecting the number of covariance matrices previously generated.

C. Alternating-Least-Squares-Based Tucker decomposition (Tucker-ALS) Algorithm for Covariance Matrix Reconstruction

The Tucker-ALS method [51] is composed of two parts: Tucker decomposition [52] and alternating least squares (ALS).

1) Tucker Decomposition: Tucker decomposition is considered as a tool for spatial compression of the modeling tensor $\mathcal{X} \in \mathbb{R}^{F_1 \times F_2 \times F_3 \times F_4 \times F_5}$, which is given by

$$\mathcal{X} \approx \mathcal{Y} \times_1 \mathbf{U}^{(1)} \times_2 \mathbf{U}^{(2)} \times_3 \mathbf{U}^{(3)} \times_4 \mathbf{U}^{(4)} \times_5 \mathbf{U}^{(5)} \tag{11}$$

where $\times_n$ is the mode-n product expressed in [53], $\mathcal{Y} \in \mathbb{R}^{R_1 \times R_2 \times R_3 \times R_4 \times R_5}$ is the core tensor, and $\mathbf{U} \in \mathbb{R}^{F_n \times R_n}$ is a series of projection matrices with orthogonal columns, where $n = 1, 2, \ldots, 5$. R is the rank of the core tensor $\mathcal{Y}$. This $\mathcal{Y}$ tensor must satisfy

$$\mathcal{Y} = \mathcal{X} \times_1 \mathbf{U}^{(1)^T} \times_2 \mathbf{U}^{(2)^T} \cdots \times_5 \mathbf{U}^{(5)^T}. \tag{12}$$

2) Alternating Least Squares: The ALS part is aimed at minimizing the following least-squares cost function [54]:

$$\min\|\mathcal{X} - \mathcal{Y} \times_1 \mathbf{U}^{(1)} \times_2 \mathbf{U}^{(2)} \times_3 \mathbf{U}^{(3)} \times_4 \mathbf{U}^{(4)} \times_5 \mathbf{U}^{(5)}\|^2 \tag{13}$$

Combining (12) and (13), the process of ALS algorithm can be described as [54, Th. 4.2]

$$\max\|\mathcal{X} \times_1 \mathbf{U}^{(1)^T} \times_2 \mathbf{U}^{(2)^T} \times_3 \mathbf{U}^{(3)^T} \times_4 \mathbf{U}^{(4)^T} \times_5 \mathbf{U}^{(5)^T}\|^2. \tag{14}$$

$\mathbf{U}^{(n)}$ can be obtained by using the alternating scheme. First, we optimize one of the matrix estimates in $\mathbf{U}^{(1)}, \mathbf{U}^{(2)}, \ldots, \mathbf{U}^{(5)}$, while keeping the other estimates of matrices unchanged. Second, we repeat the first step until the value in (13) converges. The steps of Tucker-ALS[1] are summarized in Appendix A.

One advantage of Tucker-ALS is that we can predefine the rank of the output tensor, making it suitable for a subsequent GLR test. In this regard, the following rank values were preset: $R_1 = F_1$, $R_2 = F_2$, $R_3 = R_4 = F_3 = F_4 = m$, and $R_5 = 1$. After dimensional reduction, the 5-D tensor $\mathcal{X}$ can be projected to $\mathcal{C} \in \mathbb{R}^{F_1 \times F_2 \times m \times m \times 1}$. Therefore, when considering all pixels, we can convert $\mathcal{C}$ into a new 4-D CCM $\mathbf{C} \in \mathbb{R}^{F_1 \times F_2 \times m \times m}$.

D. SHP Detection Based on the GLR Test

Under the condition of $p \geq m$, the multilooked covariance matrix derived from (2), (5), and (7) follows a complex Wishart distribution with p degrees of freedom, where p is the number of multilooking samples, and m is the dimension of the matrix.

Thanks to the linear transform property of Tucker-ALS, the decomposed matrix $\mathbf{C}$ can be assumed to follow a complex Wishart distribution [32]

$$p(\mathbf{C}|\mathbf{\Sigma}) = \frac{|\mathbf{C}|^{p-m}}{K(p,m)|\mathbf{\Sigma}|^p}\exp(-\text{tr}(\mathbf{\Sigma}^{-1}\mathbf{C})) \tag{15}$$

where $\mathbf{C} = p\hat{\mathbf{\Sigma}}$, $K(p,m) = \pi^{m(m-1)/2}\prod_{k=1}^{m}\Gamma(p-k+1)$, and $\Gamma()$ is the function defined in [55].

If matrices for different pixels are independent and identically with the same covariance matrix $\mathbf{\Sigma}$ and the same multilooking samples p, the problem of evaluating the similarity between $\mathbf{C}_1 \in \mathbf{W}_C(m, p, \mathbf{\Sigma})$ and $\mathbf{C}_2 \in \mathbf{W}_C(m, p, \mathbf{\Sigma})$ can be rephrased as the following hypothesis test:

$$H_0 : \mathbf{\Sigma}_1 = \mathbf{\Sigma}_2 = \mathbf{\Sigma}_{12}$$
$$H_1 : \mathbf{\Sigma}_1 \neq \mathbf{\Sigma}_2. \tag{16}$$

By referring to a previous study [32], a criterion Q designed specifically for the above hypothesis test can be expressed as

$$Q = \frac{(2p)^{2mp}}{p^{2mp}}\frac{|\mathbf{C}_1\mathbf{C}_2|^p}{|\mathbf{C}_1 + \mathbf{C}_2|^{2p}}. \tag{17}$$

Large values of Q indicate that $\mathbf{C}_1$ and $\mathbf{C}_2$ are likely to follow a common distribution. The probability of finding a smaller value of $-2\rho\ln Q$ can be simplified as

$$P(-2\ln Q \leq z) = P(\chi^2(m^2) \leq z). \tag{18}$$

[1][Online]. Available: https://www.tensortoolbox.org/

The similarity between two pixels can be determined by comparing their matrices. The SHP group for the reference pixel is determined by

$$w = \begin{cases} 1, & \text{if } -2\rho\ln Q \le R_{\text{thr}} \\ 0, & \text{if } -2\rho\ln Q > R_{\text{thr}} \end{cases} \quad (19)$$

where w is the similarity between the reference pixel and other pixels within the same search window, and R_{thr} is the threshold. Once the degrees of freedom m^2 and false alarm rate α are determined, R_{thr} can be obtained by looking up the chi-square distribution table.

E. Refined Estimation of Covariance Matrices by Using SHP Group

The refined matrix $\hat{\Sigma}$ for a reference pixel is estimated through multilooking scattering vectors $\mathbf{k}$ over its SHP set Ω, as determined by (19):

$$\hat{\Sigma} = \frac{1}{N} \sum_{\Omega} \mathbf{k}\mathbf{k}^H \quad (20)$$

where N is the number of pixels in the SHP set Ω.

Different kinds of matrices can be generated through utilizing the obtained SHP set. By employing the vector $\mathbf{k}$ in (1) or (6), one can obtain p polarization despeckled matrices with a size of 3×3 or 2×2. In addition, by using the vector $\mathbf{k}$ from (3), a filtered interferometric matrix with a size of $p \times p$ can be produced.

F. Selected Indicators for Filter Performance Evaluation

The performance of the proposed speckle filter is evaluated and compared with other filters adapted to the same type of input data. The assessment of the filter's performance is based on a set of well-defined indices.

1) Indices for Simulated Images: First, we use the well-known equivalent number of looks [56] (ENL) index to measure the speckle strength in homogeneous areas

$$\text{ENL} = \frac{(\text{mean}(\mathbf{INT}_{\text{f}}))^2}{\text{var}(\mathbf{INT}_{\text{f}})} \quad (21)$$

in which $\mathbf{INT}_{\text{f}}$ is the intensity value of a selected homogeneous area after filtering.

In addition, the signal-to-noise ratio (SNR) is calculated over the full image to give a global evaluation of the filtering performance

$$\text{SNR} = 10 \log_{10} \frac{\text{var}(\mathbf{Data}_{\text{t}})}{\frac{1}{N} \sum (\mathbf{Data}_{\text{o}} - \mathbf{Data}_{\text{f}})^2} \quad (22)$$

where $\mathbf{Data}_{\text{t}}$ is the true data, $\mathbf{Data}_{\text{f}}$ is the data after filtering, and $\mathbf{Data}_{\text{o}}$ is the noisy data. N is the number of pixels in the selected area. In this index, $\mathbf{Data}$ can correspond to intensity, coherence, phase, etc. A higher value of ENL and SNR indicates a better speckle reduction ability.

2) Indices for Real Images: In order to quantitatively measure the quality of filtered amplitude images, we adopted the speckle suppression index (SSI) [57] and also the more sophisticated speckle suppression and mean preservation index

(SMPI) [58] for homogeneous areas, which are calculated as

$$\text{SSI} = \frac{\text{mean}(\mathbf{INT}_{\text{o}})\sqrt{\text{var}(\mathbf{INT}_{\text{f}})}}{\text{mean}(\mathbf{INT}_{\text{f}})\sqrt{\text{var}(\mathbf{INT}_{\text{o}})}} \quad (23)$$

$$\text{SMPI} = (1 + |\text{mean}(\mathbf{INT}_{\text{o}}) - \text{mean}(\mathbf{INT}_{\text{f}})|) \frac{\sqrt{\text{var}(\mathbf{INT}_{\text{f}})}}{\sqrt{\text{var}(\mathbf{INT}_{\text{o}})}} \quad (24)$$

where subscripts f and o denote the filtered images and original noisy images, respectively. Lower values of SSI and SMPI indicate a better capability of speckle suppression and mean value preservation.

In addition, an edge enhancing index (EEI) is introduced to measure the edge preserving ability [59]

$$\text{EEI} = \frac{\sum |(\mathbf{INT}_{1\text{f}}) - (\mathbf{INT}_{2\text{f}})|}{\sum |(\mathbf{INT}_{1\text{o}}) - (\mathbf{INT}_{2\text{o}})|} \quad (25)$$

where the subscript 1f or 2f denotes the filtered intensity value on either side of the edge, and 1o or 2o represents the noisy intensity value. A higher value of EEI means better edge preservation.

III. EXPERIMENTAL RESULTS

To demonstrate the effectiveness of the proposed TD-MPF, experiments were conducted using both simulated and real PolSAR datasets. The performance of TD-MPF was compared with four mainstream algorithms in terms of their capability of suppressing speckle while preserving details. These methods are FaSHPS [25], CCM-MTF [26], MPF [28], and MSAR-BM3D filter [16].

MSAR-BM3D and FaSHPS only rely on the intensity or amplitude information of multitemporal SAR images. CCM-MTF utilizes multitemporal single-polarization SAR images to build the InSAR CCM, while MPF employs multitemporal PolSAR images and computes the multilook PolSAR CCM by averaging over the time dimension. The input of TD-MPF is a combination of CCM-MTF and MPF. Table I summarizes the characteristics of the filters used in the comparison.

To ensure comparability among the filtered results produced by the five methods, the window size for FaSHPS, CCM-MTF, MPF, and TD-MPF was fixed as 15×15. For MSAR-BM3D, the window size was set to the default recommended values (block size = 8, stack size = 32, and search window = 39).

A. Experiment With Simulated SAR Images

For conducting a reliability analysis, the ground truth must be known. With this purpose, in the first experiment, we generated a multitemporal quad-pol dataset composed of nine single-look complex PolSAR images. The simulated scene consists of four squares with different scattering characteristics, as listed in Table II. The parameters used to describe the scattering properties include: σ, which is the intensity value of HH channel; γ and ϵ, which are the scale factor of amplitude value for VV and VH in comparison to HH respectively; ρ_t, which is the complex correlation between images acquired at different time points; and ρ_p, which is the complex correlation between different polarimetric

TABLE I
CHARACTERISTICS OF THE USED FILTERS

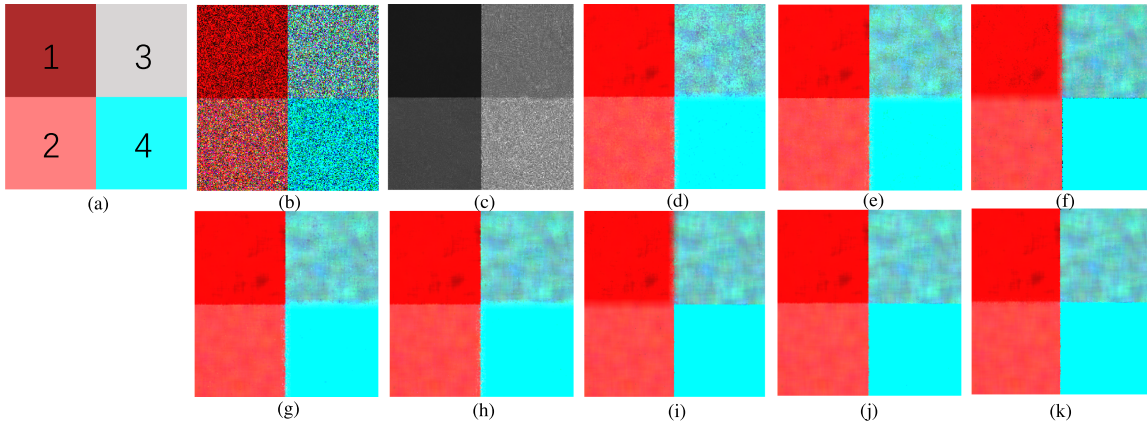|	MSAR-BM3D	FaSHPS	CCM-MTF	MPF	TD-MPF
SHP detection method	–	Confidence interval	GLR	GLR	GLR
Information used	Intensity	Amplitude	Complex	Complex	Complex
Pol-channel used	Single	Single	Single	Multi	Multi
Number of images to be applied (recommended)	≥1	≥1	≥4	≥3	≥2 (dual pol) ≥3 (quad pol)

Fig. 5. Experiment results of the simulated PolSAR dataset formed by the first image. (a) Clear. (b) Noisy. (c) MSAR-BM3D. (d) FaSHPS(VV). (e) FaSHPS(HH). (f) FaSHPS(VH). (g) CCM-MTF(VV). (h) CCM-MTF(HH). (i) CCM-MTF(VH). (j) MPF. (k) TD-MPF. Channels: R = HV, G = VV, B = HH. Note that (b) is the amplitude image. The four areas of interest are marked as 1, 2, 3, and 4 in (a).

TABLE II
DIFFERENT SIMULATED VALUES FOR FOUR AREAS

	Area 1	Area 2	Area 3	Area 4
σ	1	9	25	49
γ	1	1	1	1
ϵ	4	2	1	0.1
abs(ρ_p)	0	0.25	0.5	0.75
phase(ρ_p)	π	π	π	π
abs(ρ_t)	0.4	0.5	0.6	0.7
phase(ρ_t)	deformation signal is simulated by assuming a linear LOS velocity proportional to the intensity value.			

channels. More details about the simulation procedure are given in Appendix B.

The behavior of all different methods can be better interpreted by jointly analyzing all filters' results, presented in Fig. 5, and the SHP detection maps shown in Fig. 6. Four areas of interest are marked as 1, 2, 3, and 4 in Fig. 5(a) for the subsequent analysis. Since MSAR-BM3D is not based on a similarity evaluation between pixels, its SHP map is not shown in Fig. 6.

The accuracy in identifying SHPs has a direct impact on the filtering results. In terms of noise reduction, FaSHPS [see Fig. 6(a)–(c)] performs worse than CCM-MTF [see Fig. 6(d)–(f)] for all channels (VV, VH, and HH). The result of MPF is better than CCM-MTF, but undesired noise still exists in Area-3 and Area-4. By combining PolSAR and InSAR CCMs, the TD-MPF provides the best result in homogeneous areas.

In terms of edge preservation, VV and HH channels are sensitive to the border of Area-1, while VH channel is only good at distinguish edges of Area-4. As a result, these lines are kept well in Fig. 5, while other edges are blurred. The PolSAR filters MPF and MSAR-BM3D appear to be the best

methods for retaining structures, followed by TD-MPF. Due to the changed amplitude value of VH (compared with VV and HH), it reduces the differences between new CCMs, making it difficult to preserve pixels between Area-1 and Area-2, and between Area-1 and Area-3. As a result, like in the outputs of VH channel by FaSHPS and CCM-MTF, TD-MPF also slightly blurs the edge in Area-1, Area-2, and Area-3. This phenomenon could be alleviated by modifying the weight of the VH InSAR CCM (i.e., to make it lower), which participates in the construction of the new CCM.

To evaluate the results obtained from the simulated images, quantitative measurements of SNR and ENL are used (see Table III). Besides, the correlation between different polarimetric channels ρ_p (see Fig. 7) and the correlation between images acquired at different time instants ρ_t (see Fig. 8) are also estimated and shown in Table III for assessment. Their definitions are given in Appendix B. In Area-1, Area-3, and Area-4, ENL values for TD-MPF are better than other methods, while in Area-2, the value is comparable to MPF. Instead of estimating it independently over the four areas, the SNR value is calculated for the entire image. The TD-MPF method shows the highest SNR values, indicating the highest level of speckle reduction. To sum up, TD-MPF offers the best compromise between detail preservation and speckle reduction among all the selected filters.

B. Experiments With Real SAR Images

1) Agricultural Area With Dual-Pol TerraSAR-X Data: In the first experiment with real SAR data, eight dual-polarimetric (HH and VV) TerraSAR-X images covering an agricultural area in
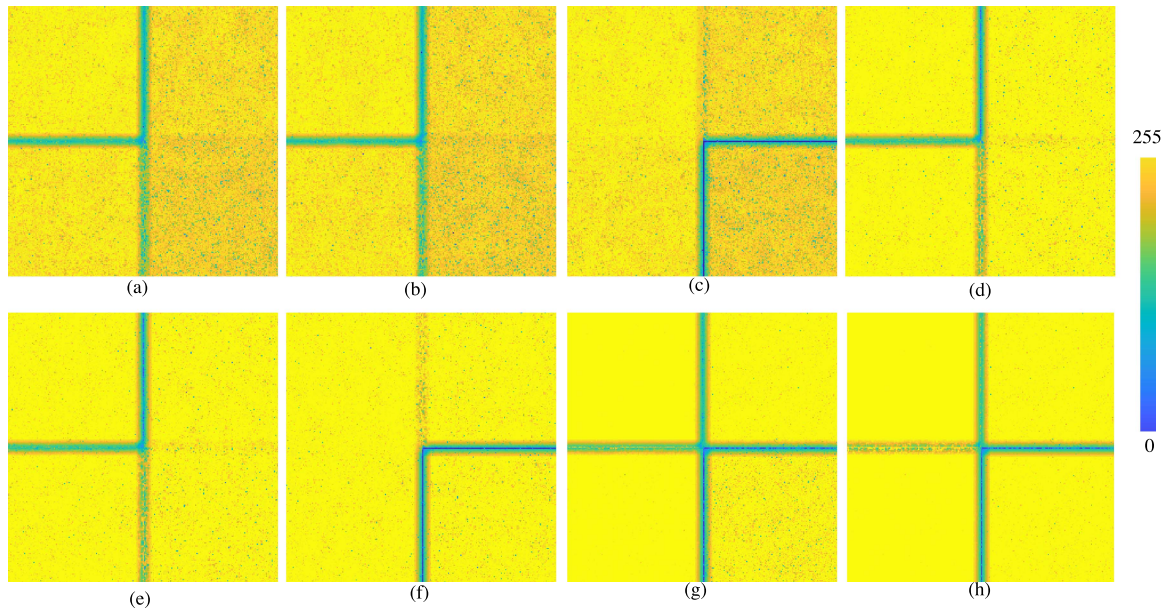
Fig. 6.   SHP map of simulated data. (a) FaSHPS(VV). (b) FaSHPS(HH). (c) FaSHPS(VH). (d) CCM-MTF(VV). (e) CCM-MTF(HH). (f) CCM-MTF(VH). (g) MPF. (h) TD-MPF.

TABLE III
QUANTITATIVE EVALUATION RESULTS FOR SIMULATED IMAGES

	Noisy	MSAR-BM3D	FaSHPS (VV)	FaSHPS (HH)	FaSHPS (VH)	CCM-MTF (VV)	CCM-MTF (HH)	CCM-MTF (VH)	MPF	TD-MPF
ENL										
Area-1	1.00	190.66	151.85	255.20	265.16	236.36	267.59	270.73	273.55	**273.64**
Area-2	1.02	41.04	83.05	183.18	145.55	153.92	172.25	156.42	**242.25**	241.71
Area-3	1.01	13.09	45.11	152.29	143.23	117.48	162.16	154.43	186.78	**189.91**
Area-4	1.01	5.55	22.96	57.87	203.09	99.21	142.88	228.06	182.35	**223.37**
SNR (dB)										
abs(ρ_p)	−3.31	–	18.30	18.45	15.79	18.95	19.98	16.01	19.12	**9.41**
abs(ρ_t)	1.65	–	22.46	17.74	21.92	23.07	23.78	23.01	23.82	**24.05**

Best value is marked in boldface. Four areas are marked in Fig. 5.

Fig. 7.   Absolute value of ρ_p. (a) Clear. (b) FaSHPS(VV). (c) FaSHPS(HH). (d) FaSHPS(VH). (e) CCM-MTF(VV). (f) CCM-MTF(HH). (g) CCM-MTF(VH). (h) MPF. (i) TD-MPF.
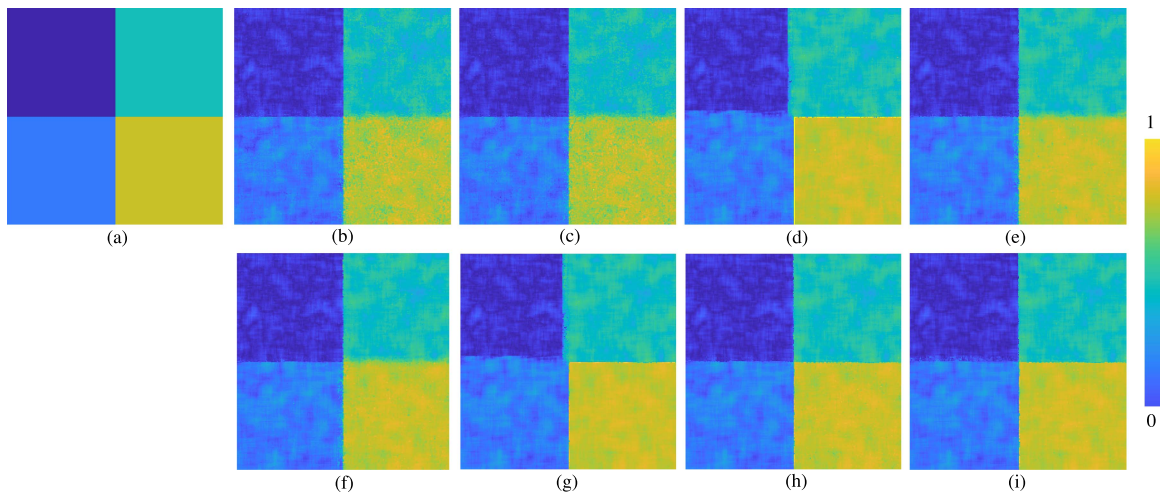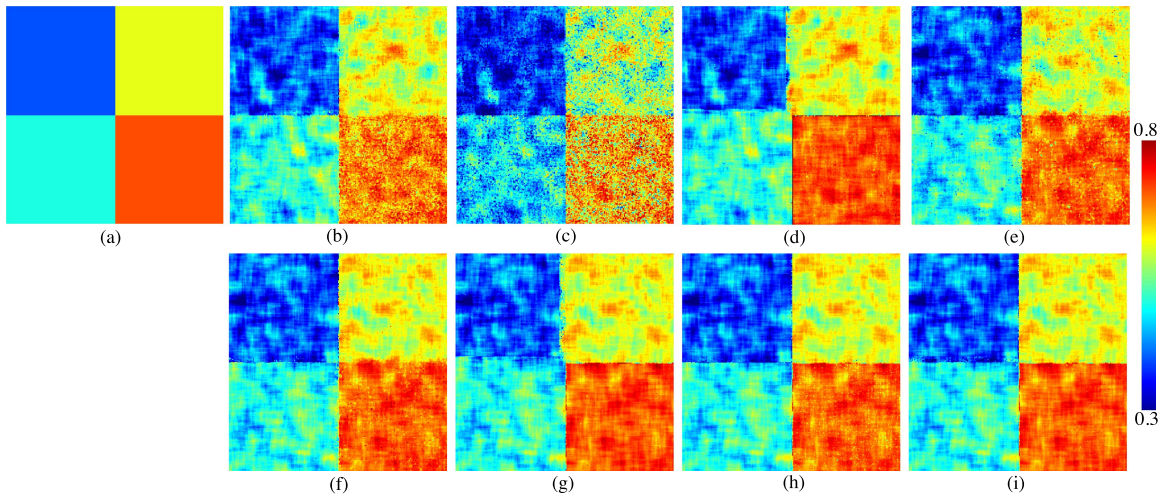
Fig. 8. Absolute value of ρ_t. (a) Clear. (b) FaSHPS(VV). (c) FaSHPS(HH). (d) FaSHPS(VH). (e) CCM-MTF(VV). (f) CCM-MTF(HH). (g) CCM-MTF(VH). (h) MPF. (i) TD-MPF.
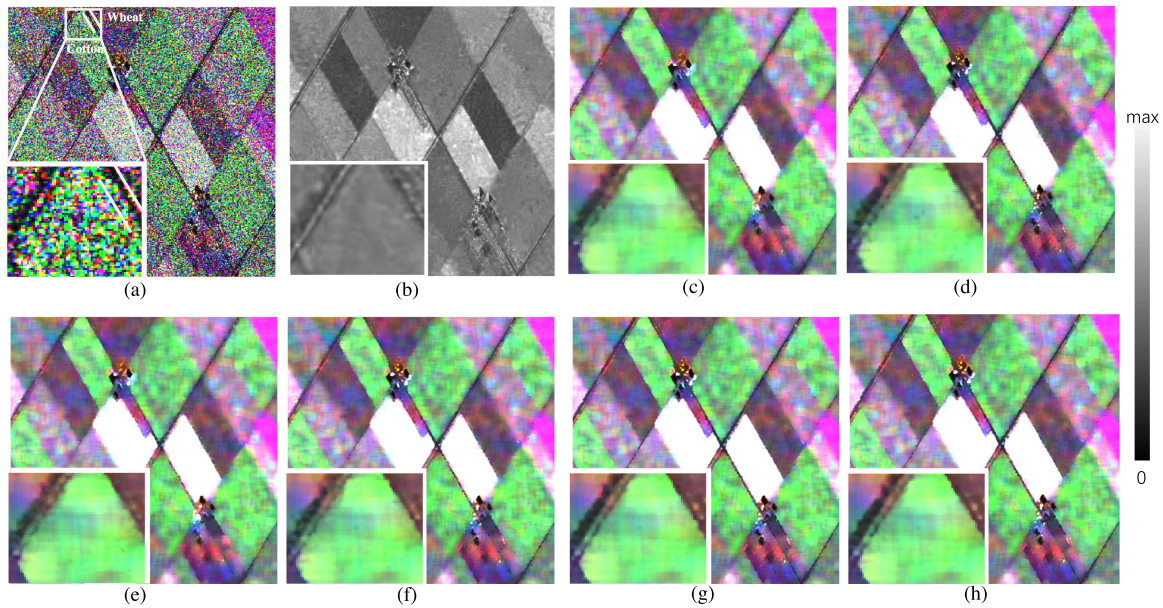

Fig. 9. Original and filtered Pauli RGB composites over the agricultural area with dual-pol (HH, VV) TerraSAR-X images. (a) Noisy. (b) MSAR-BM3D. (c) FaSHPS(VV). (d) FaSHPS(HH). (e) CCM-MTF(VV). (f) CCM-MTF(HH). (g) MPF. (h) TD-MPF. Channels: R = HH-VV, G = VV, B = HH+VV. The white lines represent pixels in the boundary of wheat and cotton. They are used to measure the effectiveness of edge preservation by different methods (see Fig. 10).

Sevilla, Spain, were used to evaluate the performance of the proposed method. These images have a spatial resolution of 6.6 m in azimuth and 2 m in range and were acquired in stripmap mode between May 25, 2017 and August 10, 2017.

The Pauli RGB composites of an image (original and filtered with the evaluated methods) are shown in Fig. 9. By visual inspection, MSAR-BM3D performs better in preserving the borders between adjacent parcels. However, the filtering performance of MSAR-BM3D inside each parcel is insufficient, as speckle is still obvious compared with other methods. On the other band, methods based on single-pol data perform well inside the parcels, but they tend to spread the edges. Apparently,

the best filtering is obtained by using polarization information, i.e., by MPF and TD-MPF.

Two polarimetric features, alpha angle and entropy (H), are used to further evaluate the impact of despeckling on the discrimination among various crop types based on their scattering characteristics [60]. Fig. 10 proves the edge preservation ability by plotting the H-alpha values measured in the boundary between wheat and cotton (the reference data of 2017 is provided by the official land parcel identification system). The two crop types are almost mixed together in FaSHPS(VV), FaSHPS(HH) and CCM-MTF(HH). Contrarily, TD-MPF and MPF show a comparable result in keeping edges, followed by CCM-MTF(VV).
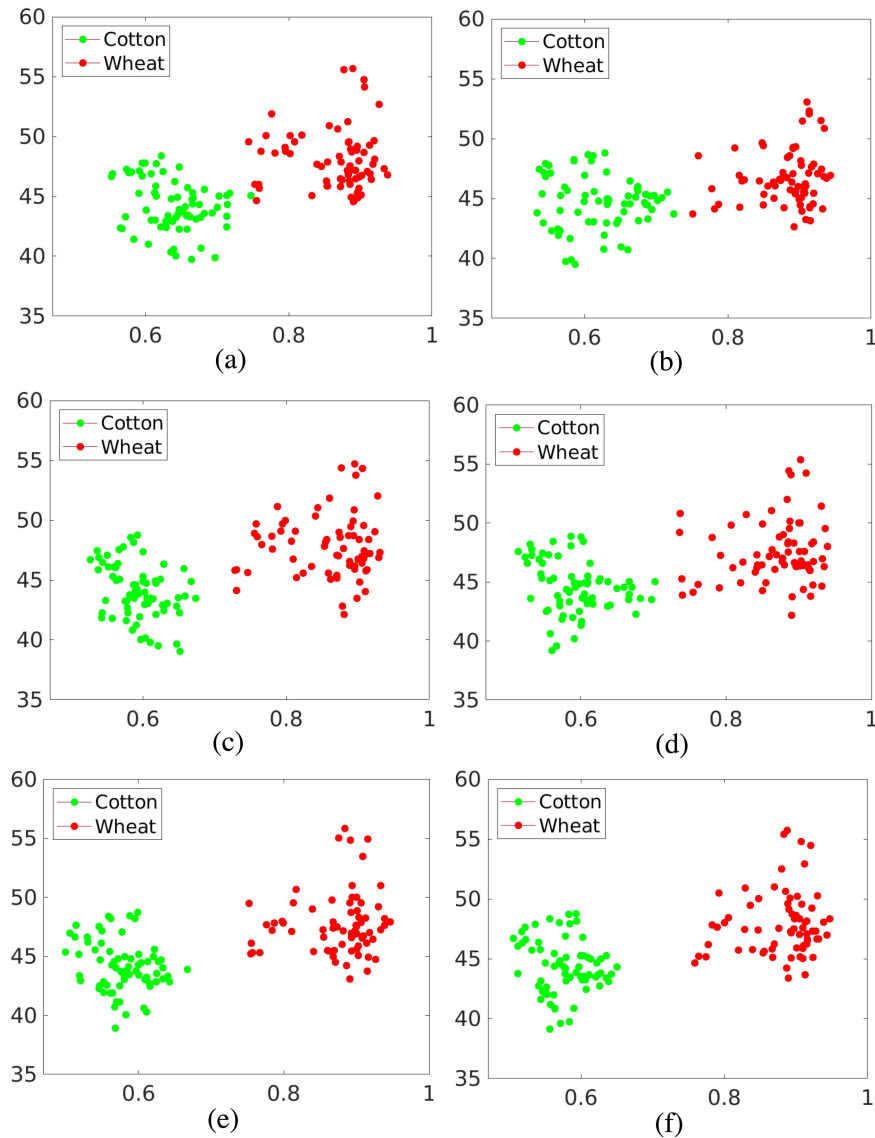
Fig. 10. H-alpha representation of the pixels in the boundary between wheat and cotton marked in Fig. 9. (a) FaSHPS(VV). (b) FaSHPS(HH). (c) CCM-MTF(VV). (d) CCM-MTF(HH). (e) MPF. (f) TD-MPF. The horizontal axis is the entropy (H), while the vertical axis is the alpha angle (in degrees).

The SHP detection map is given in Fig. 11. FaSHPS and CCM-MTF provide similar results on the border of the parcels, but CCM-MTF performs better than FaSHPS in terms of noise reduction. Fig. 11 also proves that TD-MPF and MPF are more effective in maintaining edges by selecting less pixels in areas close to different crop types. Moreover, in the homogeneous areas, the result of TD-MPF is less noisy than MPF. Therefore, TD-MPF can also achieve a better compromise between speckle suppression and detail preservation with real SAR data measured at VV and HH channels.

2) Airport Zone With Quad-Pol Radarsat-2 Data: In the second experiment, three quad-pol Radarsat-2 images acquired on January 20, 2010, February 13, 2010, and March 9, 2010 over Barcelona, Spain, were used. The beam mode is FQ9, with azimuth and range resolutions around 7.6 and 5.2 m, respectively.

The filtered results over Barcelona airport are displayed in Fig. 12. MSAR-BM3D, MPF, and TD-MPF provide clearer details at the runway and the terminal building. CCM-MTF and FaSHPS decrease the resolution to some extent. By inspecting the enlarged maps in Fig. 12, it is evident that only MPF and TD-MPF offer results comparable to the powerful MSAR-BM3D method, as the roads (black lines) are retrieved from noise. Conversely, CCM-MTF and FaSHPS lose structural information after filtering, especially in the VH channel.

The corresponding SHP identification results are shown in Fig. 13. The SHP maps in Fig. 13, obtained with only three images, demonstrate that a significant number of points in heterogeneous areas are considered as homogeneous points by FaSHPS and CCM-MTF. As a consequence, their performance is poor in heterogeneous regions. Compared with FaSHPS, CCM-MTF has better results in detect buildings since it takes advantage of

TABLE IV
STATISTICAL INDICES OF THE SELECTED HOMOGENEOUS REGION IN THE FILTERED IMAGES CORRESPONDING TO THE AIRPORT AREA WITH QUAD-POL RADARSAT-2 DATA

	Noisy	MSAR-BM3D	FaSHPS (VV)	FaSHPS (HH)	FaSHPS (VH)	CCM-MTF (VV)	CCM-MTF (HH)	CCM-MTF (VH)	MPF	TD-MPF
SSI	–	0.2146	0.1459	0.1411	0.1430	0.1464	0.1785	0.1510	0.1280	**0.1173**
$SMPI$	–	0.3471	0.1631	0.1589	0.1534	0.1658	0.2051	0.1730	0.1439	**0.1406**

The bold values indicate the best performance among the nine filters.
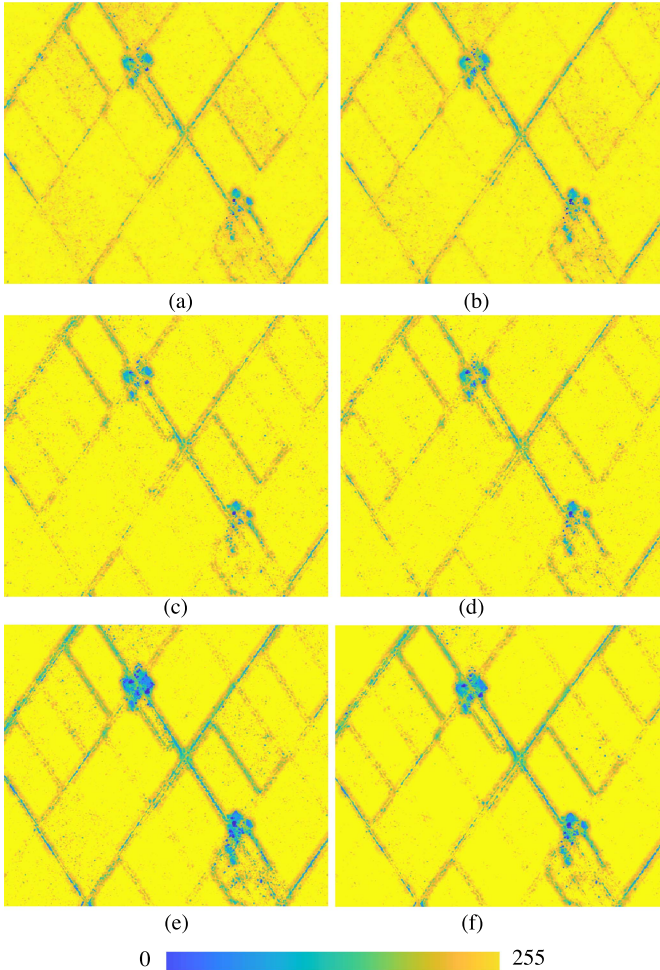

Fig. 11. SHP map of the agricultural area. (a) FaSHPS(VV). (b) FaSHPS(HH). (c) CCM-MTF(VV). (d) CCM-MTF(HH). (e) MPF. (f) TD-MPF.

the coherence value of two adjacent images, while homogeneous areas are oversmoothed with this filter. The strong ability of detail detection in Fig. 13(g) and (h) proves the effectiveness of MPF and TD-MPF, since they can effectively exploit the information gathered in multitemporal PolSAR images. Finally, TD-MPF has less residual speckle than MPF in homogeneous areas.

The quantitative assessment is presented in Table IV. Lower SSI and SMPI indicate better results in speckle reduction and mean value preservation, respectively. MSAR-BM3D achieves the highest values for SSI and SMPI, indicating its poor performance in homogeneous areas, leading to a significant difference between the filtered image and the original one. The SSI values

of CCM-MTF and FaSHPS are similar, proving their comparable noise reduction ability over the selected area. However, the SMPI value in CCM-MTF is higher than that in FaSHPS, especially in the HH channel. TD-MPF and MPF outperform other algorithms in the tested indexes. As for edge preservation, MSAR-BM3D, MPF, and TD-MPF provide similar values of EEI, indicating their comparable ability in edge preservation for real SAR data. Overall, TD-MPF produces the lowest values of SSI and SMPI but the highest value of EEI, showing its excellent performance in speckle suppression, even when processing a few images.

3) Dam Area With Dual-Pol Sentinel-1 Data: In the last experiment, 16 dual-pol (VV,VH) Sentinel-1 images acquired from May 2017 to November 2017 over the Yellow River Xiaolangdi dam of Henan province, China, were used. The observation mode is Interferometric Wide-Swath, with pixel dimensions of 13.9 and 2.3 m in azimuth and range, respectively.

The filtered amplitude images are given in Fig. 14. By visual inspection, we can see that the white line parts in FaSHPS(VH) and CCM-MTF(VH) are obviously oversmoothed. In contrast, the results from VV channel [MSAR-BM3D, FaSHPS(VV), CCM-MTF(VV)] are able to emphasize spatial structures, but still have noticeable noise in the body of the dam. The major improvement of the proposed method for this scene consists of reducing strong fluctuations while keeping important features.

By comparing the amplitude images with the map of number of identified SHP for each pixel in Fig. 15, we can see that the denoising performance of each filter comes from its SHP detection ability. FaSHPS(VV) and CCM-MTF(VV) preserve the main edge of the dam, but they cannot provide a satisfactory result in homogeneous areas due to their selection of less SHPs in these two parts. Conversely, FaSHPS(VH) and CCM-MTF(VH) select more SHPs for each pixel, leading to the spread of structures. In Fig. 15(e), obtained with the MPF method, a tradeoff performance for using VV or VH channel at the homogeneous area of the dam can be achieved, while the structure of the dam is well maintained. Finally, by combining InSAR CCM and PolSAR CCM, a better noise suppression can be achieved, while the edge of dam is still well preserved. Therefore, the proposed method is also applicable to a dataset with VV and VH channels.

IV. DISCUSSION

Experiments with simulated and real multitemporal PolSAR data have shown that InSAR CCM and PolSAR CCM exhibit different sensitivity to different targets. Therefore, using only one kind of input data, one cannot get the best result. From both visual inspection and quantitative evaluation, we concluded that the proposed TD-MPF achieves a high filtering efficiency
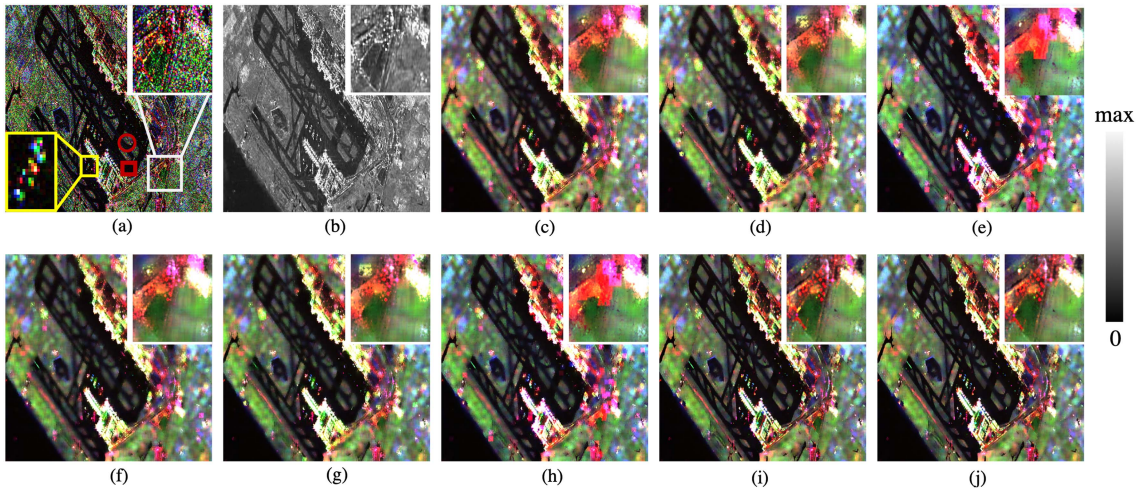
Fig. 12. Original and filtered Pauli RGB composites over the airport area with quad-pol Radarsat-2 data. (a) Noisy. (b) MSAR-BM3D. (c) FaSHPS(VV). (d) FaSHPS(HH). (e) FaSHPS(VH). (f) CCM-MTF(VV). (g) CCM-MTF(HH). (h) CCM-MTF(VH). (i) MPF. (j) TD-MPF. Channels: R = HH − VV, G = 2HV, B = HH + VV. Pixels inside the red rectangle represent an homogeneous area. Pixels inside the white rectangle are used to evaluate detail preservation capability. Statistical indices SSI and SMPI in Table IV are estimated over pixels inside the red rectangle, while EEI is estimated over pixels within the red circle.
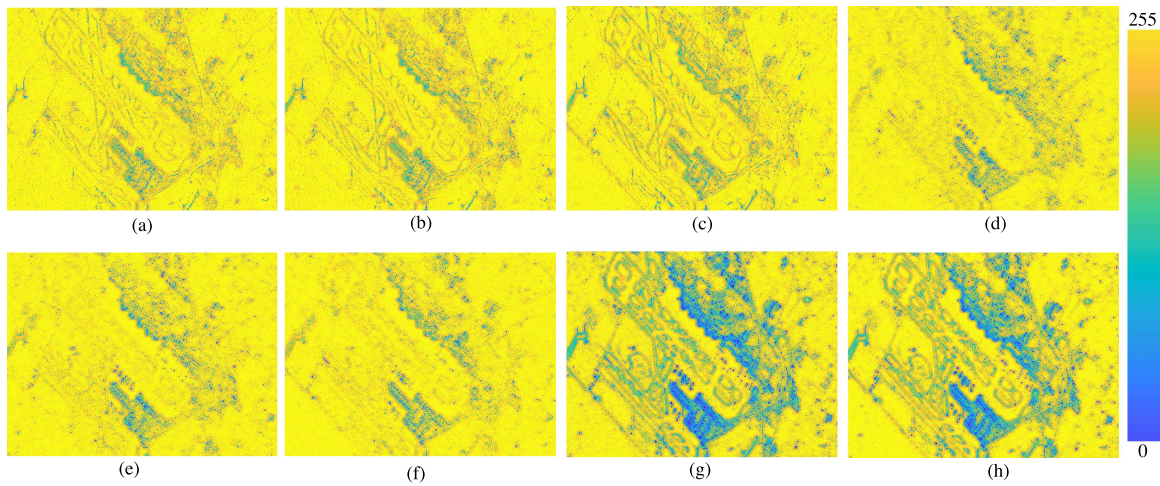

Fig. 13. SHP map of the airport area. (a) FaSHPS(VV). (b) FaSHPS(HH). (c) FaSHPS(VH). (d) CCM-MTF(VV). (e) CCM-MTF(HH). (f) CCM-MTF(VH). (g) MPF. (h) TD-MPF.
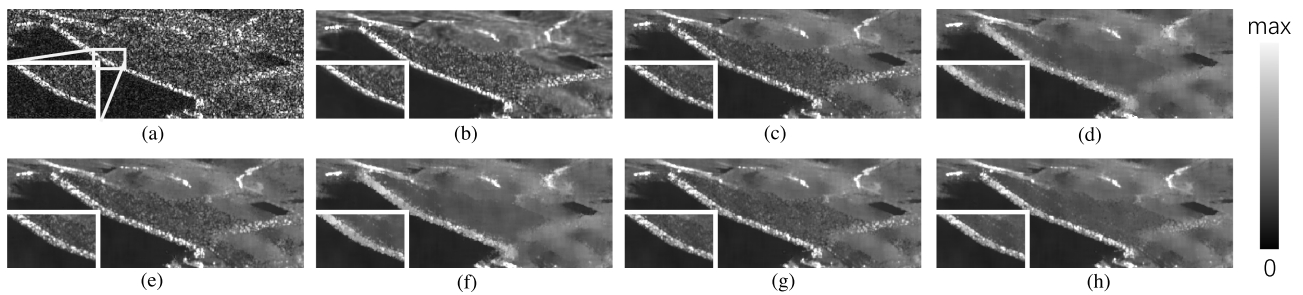

Fig. 14. Amplitude image over Xiaolangdi dam measured with Sentinel-1. (a) Noisy. (b) MSAR-BM3D. (c) FaSHPS(VV). (d) FaSHPS(VH). (e) CCM-MTF(VV). (f) CCM-MTF(VH). (g) MPF. (h) TD-MPF.
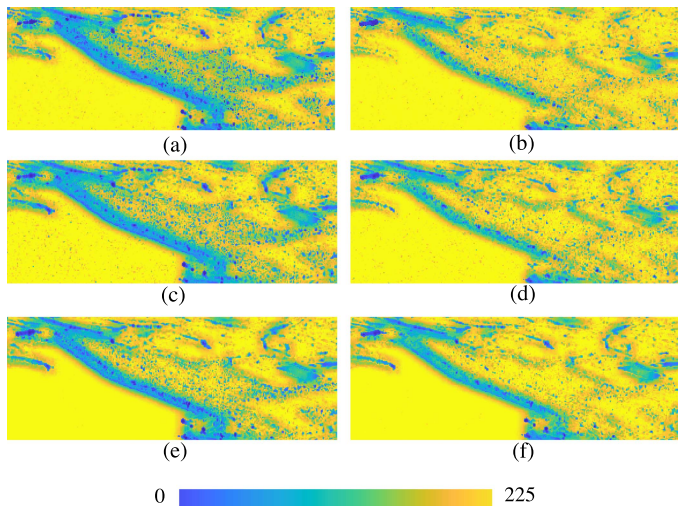
Fig. 15. SHP map of the dam area. (a) FaSHPS(VV). (b) FaSHPS(VH). (c) CCM-MTF(VV). (d) CCM-MTF(VH). (e) MPF. (f) TD-MPF.

by combining the two kinds of CCMs. The performance on detail preservation of TD-MPF is comparable to that of MPF. The improvement has been found in real datasets with different polarimetric channels, including dual-pol TerraSAR-X data (VV and HH) and Sentinel-1 data (VV and VH), and quad-pol Radarsat-2 data (VV, HH, VH, and HV). The contribution of the proposed filter is more obvious when quad-pol data are available.

A. Construction of Tensors

The performance of the proposed method could be adjusted by setting the weight of the CCMs that participate in the construction of the tensors. The strategy in this work is to compensate the InSAR CCM of the VH channel before using it and then set InSAR CCM and PolSAR CCM in an equal weight.

We use here the Radarsat-2 data over Barcelona airport and the Sentinel-1 data over Xiaolangdi dam to demonstrate the importance of the VH compensation, as well as the equal weighting of InSAR and PolSAR CCMs. The corresponding maps of number of SHPs for different cases are shown in Figs. 16 and 17, respectively.

Results show that without VH compensation [see Fig. 16(b), (d), and (f) and Fig. 17(b), (d), and (f)], the SHP maps exhibit differences compared to Fig. 16(a), (c), and (e) and Fig. 17(a), (c), and (e). This disparity is particularly evident when the weight assigned to PolSAR CCM (w_1) is low, for example, in the main part of the dam (see Fig. 17) and the homogeneous area around the airport (see Fig. 16), the results with VH compensation step are more smooth. It is also important to choose a reasonable weight for PolSAR CCM. Once the weight of PolSAR CCM is fixed, for example $w_1 = 0.2$, then the weight for each InSAR CCM equals $(1 - 0.2)/3$ for the quad-pol case and $(1 - 0.2)/2$ for the dual-pol case. When the weight for PolSAR CCM equals 0.8, the SHP detection maps will be similar to those for MPF [see Figs. 13(g) and 15(e)]. If the weight for PolSAR CCM equals 0.2, the result is close to that of CCM-MTF [see Fig. 13(d), (e), and (f) and Fig. 15(c) and (d)]. It is worth mentioning that
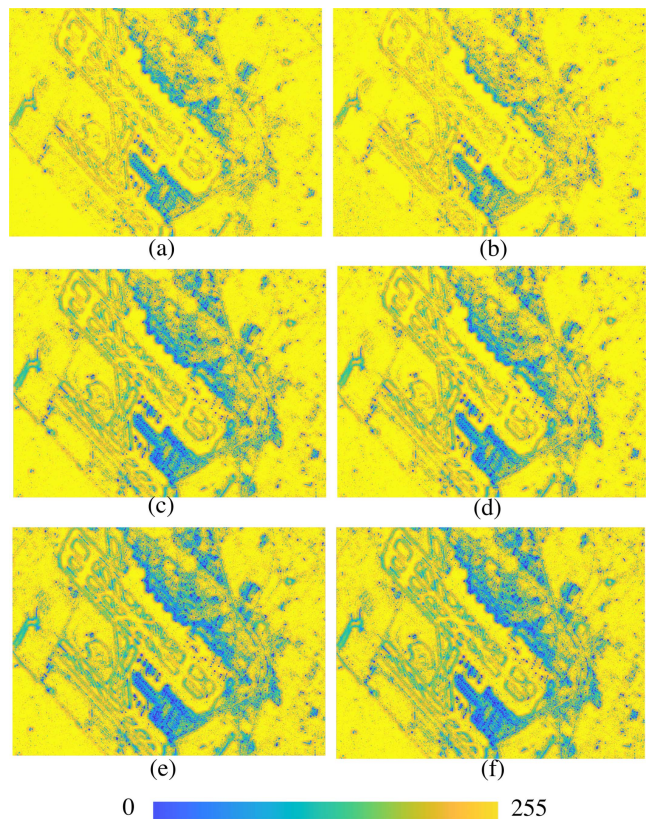
Fig. 16. SHP map of the airport area with different weight combinations. (a), (c) and (e) TD-MPF with VH compensation. (b), (d), and (f) TD-MPF without VH compensation. (a) and (b) $w_1 = 0.2$. (c) and (d) $w_1 = 0.5$. (e) and (f) $w_1 = 0.8$.
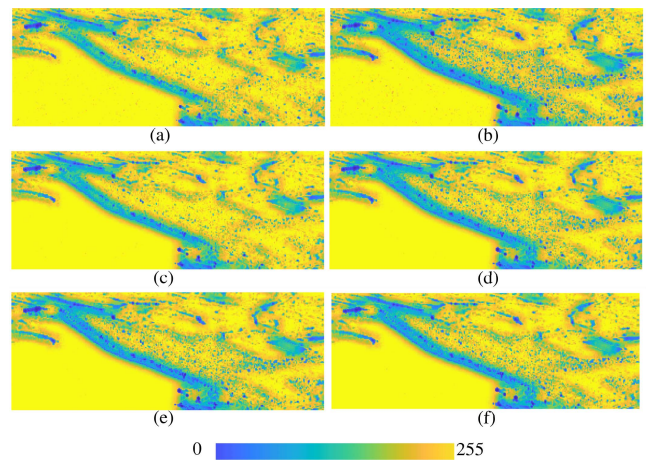
Fig. 17. SHP map of the dam area with different weight combinations. (a), (c), and (e) TD-MPF with VH compensation. (b), (d), and (f) TD-MPF without VH compensation. (a) and (b) $w_1 = 0.2$. (c) and (d) $w_1 = 0.5$. (e) and (f) $w_1 = 0.8$.

the SHP maps presented in Fig. 16 were based on only three images with a temporal baseline of approximately one month. As a result, polarimetric information dominates in this case, and retaining more polarimetric information leads to preserve more details. However, in most cases, the good compromise for detail

Fig. 18. Pauli RGB composite of the changed area in Barcelona airport (marked by yellow rectangle in Fig. 12). (a) Noisy (January 20, 2010). (b) Noisy (February 13, 2010). (c) Noisy (March 9, 2010). (d)–(l) are filtered results of the date January 20, 2010. (d) MSAR-BM3D. (e) FaSHPS(VV). (f) FaSHPS(HH). (g) FaSHPS(VH). (h) CCM-MTF(VV). (i) CCM-MTF(HH). (j) CCM-MTF(VH). (k) MPF. (l) TD-MPF. Channels: R = HH − VV, G = VV, B = HH + VV.
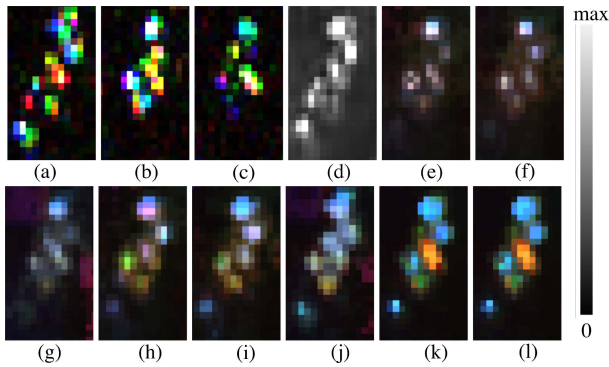
preservation and speckle reduction is obtained when the weight for PolSAR CCM equals 0.5.

B. Suitability for Short Time Series

If only a few images are available during a study period, the lack of sufficient observations reduces the efficacy of FaSHPS and CCM-MTF. In such a case, TD-MPF still can get an accurate SHP detection map by combining time series of observations from each channel, thus benefitting edge preservation and speckle reduction. Many potential applications may benefit from the improved estimation of the identified SHP sets and the estimated CCM, for example, classification with short time series, DInSAR with short time series, etc. Since the proposed algorithm entails a multilook along the temporal dimension, it is not suitable for applications with long-time series, in which specific events and changes of the scene located at particular instants need to be preserved.

C. Detection of Temporary Targets

Fig. 18 is provided to analyze the filters' performance when target distribution changes. In the first acquired image (January 20, 2010), bright targets were observed near the terminal, while in the second (February 13, 2010) and third (March 9, 2010) images, the number of bright targets decreased. The results generated by the different filters for the first image are shown in Fig. 18(d)–(h) and (l). FaSHPs [see Fig. 18(e), (f), and (g)] failed to preserve the bright scatters that appeared in the first date. Based on the strategy of averaging the CCMs, CCM-MTF, MPF, and TD-MPF can capture these changes, which suggest that these three methods can detect bright targets that partially exist in the data stack along temporal dimension.

D. Computation Efficiency

Finally, we compare the execution time for the filters by using eight dual-pol images and nine quad-pol images of size 256×256. Details are given in Table V. The computation time

TABLE V
COMPARISON OF THE COMPUTATION TIME FOR WINDOW SIZE 15×15 OVER 256×256 PIXELS

	MSAR-BM3D	FaSHPS	CCM-MTF	MPF	TD-MPF
Dual-pol	9.87s	2.37 s	7.06 s	7.49 s	9.53 s
Quad-pol	–	2.70 s	20.75 s	22.02 s	25.98 s

of MSAR-BM3D and FaSHPS depends on both image size and temporal dimension. Only dual-pol case is shown in MSAR-BM3D because it can only deal with dataset with temporal dimension 2^n. The time consumption for CCM-MTF, MPF and TD-MPF relays on image size and matrix size; as a result, quad-pol data $256 \times 256 \times 3 \times 3$ require longer processing time than dual-pol data $256 \times 256 \times 2 \times 2$. Because of the special design of FaSHPS, it results as the fastest method. For the proposed methods, as only one tensor decomposition step is added before the similarity test, the computational cost of TD-MPF is similar to that of other filters based on the GLR test. The execution time is measured on a workstation equipped with an Intel Xeon CPU at 3.50 GHz and 16 GB of RAM.

V. CONCLUSION

In this article, a novel multitemporal PolSAR filtering method named TD-MPF was proposed by integrating InSAR CCM and PolSAR CCM through tensor decomposition. The proposed method was compared with different filters, including MSAR-BM3D, FaSHPS, CCM-MTF, and MPF. Experiments using multitemporal simulated and real PolSAR images demonstrated the robust performance of TD-MPF at different scenarios for edge preservation and speckle suppression. The proposed TD-MPF is suitable for processing both quad-pol and dual-pol SAR data stacks. As a result, the improved estimation of InSAR CCM or PolSAR CCM may benefit a number of potential applications, such as deformation or crop monitoring, classification, and change detection.

APPENDIX A
PSEUDOCODE OF TUCKER-ALS

APPENDIX B
SIMULATION OF MULTITEMPORAL POLSAR IMAGES

The simulated dataset has been generated according to the complex Gaussian polarimetric model, for each pixel in the p-dimensional multitemporal PolSAR dataset, assuming a reflection symmetric target, which has a covariance matrix $\mathbf{C}$ of size $3p \times 3p$. From a matrix $\mathbf{C}$, we can obtain p SLC SAR images for each polarimetric channel using the procedure introduced in [61]

$$\mathbf{C} = \begin{bmatrix} \boldsymbol{\Sigma}_{HH} & \mathbf{O} & \boldsymbol{\Sigma}_{HHVV} \\ \mathbf{O} & \boldsymbol{\Sigma}_{VH} & \mathbf{O} \\ \boldsymbol{\Sigma}_{HHVV}^* & \mathbf{O} & \boldsymbol{\Sigma}_{VV} \end{bmatrix}. \tag{26}$$

The matrices $\boldsymbol{\Sigma}_{HH}, \boldsymbol{\Sigma}_{VV}$, and $\boldsymbol{\Sigma}_{VH}$ in the diagonal are the interference matrices of size $p \times p$. The relations of the three channels

---

Algorithm 1: Tucker-ALS.

Input: $\mathcal{X} \in \mathbb{R}^{F_1 \times F_2 \times F_3 \times F_4 \times F_5}$ − tensor
$\quad R_n$ − Low rank approximation dimension
Output: $\mathcal{C} \in \mathbb{R}^{F_1 \times F_2 \times F_3 \times F_4 \times F_5}$ − tensor
step1: Initial values for $\mathbf{U}_0^{(n)} \in \mathbb{R}^{F_n \times R_n}$, in which the column
form an orthonormal basis for the dominant R_n-dimension left
singular subspace of $\mathcal{X}^{(n)} (2 \leq n \leq 5)$.
step2: Iterate until convergence
$\quad \tilde{\mathcal{Y}}_{k+1}^{(1)} = \mathcal{X} \times_2 \mathbf{U}^{(2)^T} \times_3 \mathbf{U}^{(3)^T} \times_4 \mathbf{U}^{(4)^T} \times_5 \mathbf{U}^{(5)^T}$
$\quad$ Maximize over $\mathbf{U}^{(1)} \in \mathbb{R}^{I_1 \times R_1}$ with $\mathbf{U}^{(1)^T} \mathbf{U}^{(1)} = \mathbf{I}$
$\quad \max h(\mathbf{U}^{(1)}) = \max \|\tilde{\mathcal{Y}}_{k+1}^{(1)} \times_1 \mathbf{U}^{(1)^T}\| = h(\mathbf{U}_{\max}^{(1)})$
$\quad \mathbf{U}_{k+1}^{(1)} = \mathbf{U}_{\max}^{(1)}$

$\quad \dddot{\mathcal{Y}}_{k+1}^{(5)} = \mathcal{X} \times_1 \mathbf{U}^{(1)^T} \times_2 \mathbf{U}^{(2)^T} \times_3 \mathbf{U}^{(3)^T} \times_4 \mathbf{U}^{(4)^T}$
$\quad$ Maximize over $\mathbf{U}^{(5)} \in \mathbb{R}^{I_5 \times R_5}$ with $\mathbf{U}^{(5)^T} \mathbf{U}^{(5)} = \mathbf{I}$
$\quad \max h(\mathbf{U}^{(5)}) = \max \|\tilde{\mathcal{Y}}_{k+1}^{(5)} \times_1 \mathbf{U}^{(5)^T}\| = h(\mathbf{U}_{\max}^{(5)})$
$\quad \mathbf{U}_{k+1}^{(5)} = \mathbf{U}_{\max}^{(5)}$
$\quad$ Converged values: $\mathbf{U}^{(1)}, \mathbf{U}^{(2)}, \ldots, \mathbf{U}^{(5)}$
step3: : $\mathcal{C} = \mathcal{X} \times_5 \mathbf{U}^{(5)^T}$

---

are

$$\mathbf{\Sigma}_{VV} = \gamma^2 \cdot \mathbf{\Sigma}_{HH} \tag{27}$$

$$\mathbf{\Sigma}_{VH} = \epsilon^2 \cdot \mathbf{\Sigma}_{HH} \tag{28}$$

in which γ and ϵ are the scale factors of amplitude value for VV and VH channel, respectively. $\mathbf{\Sigma}_{HH}$ is defined as

$$\mathbf{\Sigma}_{HH} = \mathbf{\Sigma}_{HH} = \begin{bmatrix} \sigma & \rho_t \sigma \cdots\cdots\cdots\cdots \rho_t \sigma \\ \rho_t^* \sigma & \sigma \cdots\cdots\cdots\cdots \rho_t \sigma \\ \vdots & \vdots & \ddots & \vdots \\ \vdots & \vdots & & \ddots \\ \rho_t^* \sigma & \rho_t^* \sigma \cdots\cdots\cdots\cdots \sigma \end{bmatrix} \tag{29}$$

where * denotes the complex conjugate, σ is the intensity value of the images, and ρ_t is the complex correlation between images acquired at different time points.

The matrices $\mathbf{\Sigma}_{HHVV}$ and $\mathbf{\Sigma}_{HHVV}^*$ in the off-diagonal of (26) correspond to the polarimetric relation between HH and VV channels, which is defined as

$$\mathbf{\Sigma}_{HHVV} = \mathbf{\Sigma}_{HHVV} = \begin{bmatrix} \rho_p \sigma & \rho_t \rho_p \sigma \cdots\cdots\cdots\cdots \rho_t \rho_p \sigma \\ \rho_t^* \rho_p^* \sigma & \rho_p \sigma \cdots\cdots\cdots\cdots \rho_t \rho_p \sigma \\ \vdots & \vdots & \ddots & \vdots \\ \vdots & \vdots & & \ddots \\ \rho_t^* \rho_p^* \sigma & \rho_t^* \rho_p^* \sigma \cdots\cdots\cdots\cdots \rho_p \sigma \end{bmatrix} \tag{30}$$

where ρ_p is the complex correlation between different polarimetric channels.

In (29) and (30), we set different ρ_t, ρ_p, σ, γ, and ϵ for the four areas marked in Fig. 5(a), using the values listed in Table II.

REFERENCES

[1] I. Hajnsek and Y.-L. Desnos, *Polarimetric Synthetic Aperture Radar. Principles and Application*. New York, NY, USA: Springer, 2021.

[2] J. Dong, S. Lai, N. Wang, Y. Wang, L. Zhang, and M. Liao, "Multi-scale deformation monitoring with Sentinel-1 InSAR analyses along the middle route of the south-north water diversion project in China," *Int. J. Appl. Earth Observ. Geoinf.*, vol. 100, 2021, Art. no. 102324.

[3] Q. Li, W. Wang, J. Wang, J. Zhang, and D. Geng, "Exploring the relationship between InSAR coseismic deformation and earthquake-damaged buildings," *Remote Sens. Environ.*, vol. 262, 2021, Art. no. 112508.

[4] Y. Wang et al., "Refined InSAR tropospheric delay correction for wide-area landslide identification and monitoring," *Remote Sens. Environ.*, vol. 275, 2022, Art. no. 113013.

[5] F. Sica, A. Pulella, M. Nannini, M. Pinheiro, and P. Rizzoli, "Repeat-pass SAR interferometry for land cover classification: A methodology using Sentinel-1 short-time-series," *Remote Sens. Environ.*, vol. 232, 2019, Art. no. 111277.

[6] J.-S. Lee, "Digital image enhancement and noise filtering by use of local statistics," *IEEE Trans. Pattern Anal. Mach. Intell.*, vol. PAMI-2, no. 2, pp. 165–168, Mar. 1980.

[7] J.-S. Lee, "Digital image smoothing and the sigma filter," *Comput. Vis. Graph. Image Process.*, vol. 24, no. 2, pp. 255–269, 1983.

[8] D. T. Kuan, A. A. Sawchuk, T. C. Strand, and P. Chavel, "Adaptive noise smoothing filter for images with signal-dependent noise," *IEEE Trans. Pattern Anal. Mach. Intell.*, vol. PAMI-7, no. 2, pp. 165–177, Mar. 1985.

[9] V. S. Frost, J. A. Stiles, K. S. Shanmugan, and J. C. Holtzman, "A model for radar images and its application to adaptive digital filtering of multiplicative noise," *IEEE Trans. Pattern Anal. Mach. Intell.*, vol. PAMI-4, no. 2, pp. 157–166, Mar. 1982.

[10] M. Yahia, T. Ali, M. M. Mortula, R. Abdelfattah, S. E. Mahdy, and N. S. Arampola, "Enhancement of SAR speckle denoising using the improved iterative filter," *IEEE J. Sel. Topics Appl. Earth Observ. Remote Sens.*, vol. 13, pp. 859–871, 2020.

[11] M. Yahia, T. Ali, M. M. Mortula, R. Abdelfattah, and S. E. Mahdy, "Polarimetric SAR speckle reduction by hybrid iterative filtering," *IEEE Access*, vol. 8, pp. 89603–89616, 2020.

[12] G. Vasile, E. Trouve, J.-S. Lee, and V. Buzuloiu, "Intensity-driven adaptive-neighborhood technique for polarimetric and interferometric SAR parameters estimation," *IEEE Trans. Geosci. Remote Sens.*, vol. 44, no. 6, pp. 1609–1621, Jun. 2006.

[13] C.-A. Deledalle, L. Denis, and F. Tupin, "Iterative weighted maximum likelihood denoising with probabilistic patch-based weights," *IEEE Trans. Image Process.*, vol. 18, no. 12, pp. 2661–2672, Dec. 2009.

[14] S. Parrilli, M. Poderico, C. V. Angelino, and L. Verdoliva, "A nonlocal SAR image denoising algorithm based on LLMMSE wavelet shrinkage," *IEEE Trans. Geosci. Remote Sens.*, vol. 50, no. 2, pp. 606–616, Feb. 2012.

[15] J. Zhang, J. Chen, H. Yu, D. Yang, X. Xu, and M. Xing, "Learning an SAR image despeckling model via weighted sparse representation," *IEEE J. Sel. Topics Appl. Earth Observ. Remote Sens.*, vol. 14, pp. 7148–7158, 2021.

[16] G. Chierchia, M. El Gheche, G. Scarpa, and L. Verdoliva, "Multitemporal SAR image despeckling based on block-matching and collaborative filtering," *IEEE Trans. Geosci. Remote Sens.*, vol. 55, no. 10, pp. 5467–5480, Oct. 2017.

[17] N. Gasnier, L. Denis, and F. Tupin, "On the use and denoising of the temporal geometric mean for SAR time series," *IEEE Geosci. Remote Sens. Lett.*, vol. 19, 2022, Art. no. 4008205.

[18] C.-A. Deledalle, L. Denis, S. Tabti, and F. Tupin, "MuLoG, or how to apply Gaussian denoisers to multi-channel SAR speckle reduction?," *IEEE Trans. Image Process.*, vol. 26, no. 9, pp. 4389–4403, Sep. 2017.

[19] W. Zhao, C.-A. Deledalle, L. Denis, H. Maître, J.-M. Nicolas, and F. Tupin, "Ratio-based multitemporal SAR images denoising: RABASAR," *IEEE Trans. Geosci. Remote Sens.*, vol. 57, no. 6, pp. 3552–3565, Jun. 2019.

[20] H. Lin, Y. Zhuang, Y. Huang, and X. Ding, "Unpaired speckle extraction for SAR despeckling," *IEEE Trans. Geosci. Remote Sens.*, vol. 61, 2023, Art. no. 5201014.

[21] F. Lattari, B. G. Leon, F. Asaro, A. Rucci, C. Prati, and M. Matteucci, "Deep learning for SAR image despeckling," *Remote Sens.*, vol. 11, no. 13, 2019, Art. no. 1532.

[22] L. Denis, E. Dalsasso, and F. Tupin, "A review of deep-learning techniques for SAR image restoration," in *Proc. IEEE Int. Geosci. Remote Sens. Symp.*, 2021, pp. 411–414.

[23] I. Meraoumia, E. Dalsasso, L. Denis, and F. Tupin, "Fast strategies for multi-temporal speckle reduction of Sentinel-1 GRD images," in *Proc. IEEE Int. Geosci. Remote Sens. Symp.*, 2022, pp. 687–690.

[24] A. Ferretti, A. Fumagalli, F. Novali, C. Prati, F. Rocca, and A. Rucci, "A new algorithm for processing interferometric data-stacks: SqueeSAR," *IEEE Trans. Geosci. Remote Sens.*, vol. 49, no. 9, pp. 3460–3470, Sep. 2011.

[25] M. Jiang, X. Ding, R. F. Hanssen, R. Malhotra, and L. Chang, "Fast statistically homogeneous pixel selection for covariance matrix estimation for multitemporal InSAR," *IEEE Trans. Geosci. Remote Sens.*, vol. 53, no. 3, pp. 1213–1224, Mar. 2015.

[26] J. Dong, M. Liao, L. Zhang, and J. Gong, "A unified approach of multitemporal SAR data filtering through adaptive estimation of complex covariance matrix," *IEEE Trans. Geosci. Remote Sens.*, vol. 56, no. 9, pp. 5320–5333, Sep. 2018.

[27] K. Goel and N. Adam, "A distributed scatterer interferometry approach for precision monitoring of known surface deformation phenomena," *IEEE Trans. Geosci. Remote Sens.*, vol. 52, no. 9, pp. 5454–5468, Sep. 2013.

[28] V. D. Navarro-Sanchez and J. M. Lopez-Sanchez, "Spatial adaptive speckle filtering driven by temporal polarimetric statistics and its application to PSI," *IEEE Trans. Geosci. Remote Sens.*, vol. 52, no. 8, pp. 4548–4557, Aug. 2014.

[29] M. A. Stephens, "Use of the Kolmogorov-Smirnov, Cramer-Von Mises and related statistics without extensive tables," *J. Roy. Statist. Soc.*, vol. 32, no. 1, pp. 115–122, 1970.

[30] J. Bao, X. Luo, G. Liu, L. Chang, and S. Wu, "An improved distributed scatterers extraction algorithm for monitoring tattered ground surface subsidence with DSInSAR: A case study of loess landform in Tongren county," *Int. J. Appl. Earth Observ. Geoinf.*, vol. 99, no. 5827, 2021, Art. no. 102322.

[31] C. Zhao et al., "A statistically homogeneous pixel selection approach for adaptive estimation of multitemporal InSAR covariance matrix," *Int. J. Appl. Earth Observ. Geoinf.*, vol. 110, 2022, Art. no. 102792.

[32] K. Conradsen, A. Nielsen, J. Schou, and H. Skriver, "A test statistic in the complex Wishart distribution and its application to change detection in polarimetric SAR data," *IEEE Trans. Geosci. Remote Sens.*, vol. 41, no. 1, pp. 4–19, Jan. 2003.

[33] J.-S. Lee, M. R. Grunes, and G. De Grandi, "Polarimetric SAR speckle filtering and its implication for classification," *IEEE Trans. Geosci. Remote Sens.*, vol. 37, no. 5, pp. 2363–2373, Sep. 1999.

[34] C. Lopez-Martinez and X. Fabregas, "Polarimetric SAR speckle noise model," *IEEE Trans. Geosci. Remote Sens.*, vol. 41, no. 10, pp. 2232–2242, Oct. 2003.

[35] C. Lopez-Martinez and X. Fabregas, "Model-based polarimetric SAR speckle filter," *IEEE Trans. Geosci. Remote Sens.*, vol. 46, no. 11, pp. 3894–3907, Nov. 2008.

[36] R. I. Leonid, S. Osher, and E. Fatemi, "Nonlinear total variation based noise removal algorithms," *Phys. D: Nonlinear Phenomena*, vol. 60, no. 1, pp. 259–268, 1992.

[37] X. Nie, H. Qiao, and B. Zhang, "A variational model for PolSAR data speckle reduction based on the Wishart distribution," *IEEE Trans. Image Process.*, vol. 24, no. 4, pp. 1209–1222, Apr. 2015.

[38] X. Nie, H. Qiao, B. Zhang, and X. Huang, "A nonlocal TV-based variational method for PolSAR data speckle reduction," *IEEE Trans. Image Process.*, vol. 25, no. 6, pp. 2620–2634, Jun. 2016.

[39] A. Alonso-Gonzalez, C. Lopez-Martinez, and P. Salembier, "Filtering and segmentation of polarimetric SAR data based on binary partition trees," *IEEE Trans. Geosci. Remote Sens.*, vol. 50, no. 2, pp. 593–605, Feb. 2012.

[40] G. Wang et al., "Distributed scatterer processing based on binary partition trees with multi-baseline PolInSAR data," *Remote Sens.*, vol. 14, no. 21, 2022, Art. no. 5367.

[41] D. Tucker and L. C. Potter, "Polarimetric SAR despeckling with convolutional neural networks," *IEEE Trans. Geosci. Remote Sens.*, vol. 60, 2022, Art. no. 5110712.

[42] M. Yahia, T. Ali, M. M. Mortula, R. Abdelfattah, and S. Elmahdy, "Polarimetric SAR image filtering by infinite number of looks prediction technique," *IEEE J. Sel. Topics Appl. Earth Observ. Remote Sens.*, vol. 14, pp. 4167–4184, 2021.

[43] J. Chen, Y. Chen, W. An, Y. Cui, and J. Yang, "Nonlocal filtering for polarimetric SAR data: A pretest approach," *IEEE Trans. Geosci. Remote Sens.*, vol. 49, no. 5, pp. 1744–1754, May 2011.

[44] C.-A. Deledalle, L. Denis, F. Tupin, A. Reigber, and M. Jäger, "NL-SAR: A unified nonlocal framework for resolution-preserving (Pol)(In)SAR denoising," *IEEE Trans. Geosci. Remote Sens.*, vol. 53, no. 4, pp. 2021–2038, Apr. 2015.

[45] C.-A. Deledalle, L. Denis, L. Ferro-Famil, J.-M. Nicolas, and F. Tupin, "Multi-temporal speckle reduction of polarimetric SAR images: A ratio-based approach," in *Proc. IEEE Int. Geosci. Remote Sens. Symp.*, 2019, pp. 899–902.

[46] G. Wang et al., "A phase optimization method for DS-InSAR based on SKP decomposition from quad-polarized data," *IEEE Geosci. Remote Sens. Lett.*, vol. 19, 2022, Art. no. 4008805.

[47] D. Ai, G. Duan, X. Han, and Y.-W. Chen, "Generalized N-dimensional independent component analysis and its application to multiple feature selection and fusion for image classification," *Neurocomputing*, vol. 103, pp. 186–197, 2013.

[48] M. Tao, F. Zhou, Y. Liu, and Z. Zhang, "Tensorial independent component analysis-based feature extraction for polarimetric SAR data classification," *IEEE Trans. Geosci. Remote Sens.*, vol. 53, no. 5, pp. 2481–2495, May 2015.

[49] L. Zhang, L. Zhang, D. Tao, and X. Huang, "Tensor discriminative locality alignment for hyperspectral image spectral–spatial feature extraction," *IEEE Trans. Geosci. Remote Sens.*, vol. 51, no. 1, pp. 242–256, Jan. 2013.

[50] J. Kang, Y. Wang, M. Schmitt, and X. X. Zhu, "Object-based multipass InSAR via robust low-rank tensor decomposition," *IEEE Trans. Geosci. Remote Sens.*, vol. 56, no. 6, pp. 3062–3077, Jun. 2018.

[51] J. D. Carroll and J.-J. Chang, "Analysis of individual differences in multidimensional scaling via an N-way generalization of "Eckart-Young" decomposition," *Psychometrika*, vol. 35, no. 3, pp. 283–319, 1970.

[52] L. Tucker and C. Harris, *Implications of Factor Analysis of Three Way Matrices for Measurements of Change*. Madison, WI, USA: Univ. Wisconsin Press, 1963.

[53] T. G. Kolda and B. W. Bader, "Tensor decompositions and applications," *SIAM Rev.*, vol. 51, no. 3, pp. 455–500, 2009.

[54] L. De Lathauwer, B. De Moor, and J. Vandewalle, "On the best rank-1 and rank-(r1, r2,.. ., rn) approximation of higher-order tensors," *SIAM J. Matrix Anal. Appl.*, vol. 21, no. 4, pp. 1324–1342, 2000.

[55] N. R. Goodman, "Statistical analysis based on a certain multivariate complex Gaussian distribution (an introduction)," *Ann. Math. Statist.*, vol. 34, no. 1, pp. 152–177, 1963.

[56] L. Gagnon and A. Jouan, "Speckle filtering of SAR images: A comparative study between complex-wavelet-based and standard filters," *Proc. SPIE*, vol. 3169, pp. 80–91, 1997.

[57] J. S. Lee, L. Jurkevich, P. Dewaele, P. Wambacq, and A. Oosterlinck, "Speckle filtering of synthetic aperture radar images: A review," *Remote Sens. Rev.*, vol. 8, no. 4, pp. 313–340, 1994.

[58] A. Shamsoddini and J. C. Trinder, "Image texture preservation in speckle noise suppression," *Proc. Int. Arch. Photogrammetry Remote Sens. Spatial Inf. Sci.*, vol. 38, no. 7A, pp. 239–244, 2010.

[59] Y. Sheng and Z.-G. Xia, "A comprehensive evaluation of filters for radar speckle suppression," in *Proc. Int. Geosci. Remote Sens. Symp.*, 1996, pp. 1559–1561.

[60] S. Cloude and E. Pottier, "An entropy based classification scheme for land applications of polarimetric SAR," *IEEE Trans. Geosci. Remote Sens.*, vol. 35, no. 1, pp. 68–78, Jan. 1997.

[61] J.-S. Lee, M. R. Grunes, and R. Kwok, "Classification of multi-look polarimetric SAR imagery based on complex Wishart distribution," *Int. J. Remote Sens.*, vol. 15, no. 11, pp. 2299–2311, 1994.

Jiayin Luo received the B.S. degree from Northeastern University, Shenyang, China, in 2018, and the M.S. degree from the State Key Laboratory of Information Engineering in Surveying, Mapping and Remote Sensing, Wuhan University, China, in 2020, both in geomatics engineering. She is currently working toward the Ph.D. degree in computer science with the University of Alicante, Alicante, Spain.

Her research interests include polarimetric and interferometric techniques.

Lu Zhang received the B.Eng. and M.Eng. degrees in computer science and technology from the Wuhan University of Hydraulic and Electrical Engineering, Wuhan, China, in 1997 and 2000, respectively, and the Ph.D. degree in photogrammetry and remote sensing from Wuhan University, Wuhan, in 2005.

From 2005 to 2007, he was a Postdoctoral Research Fellow with the Institute of Space and Earth Information Science, Chinese University of Hong Kong, Hong Kong. Since 2007, he has been with the State Key Laboratory of Surveying, Mapping and Remote Sensing, Wuhan University, where he became a Full Professor in 2013. He was involved in several research projects funded by the National Natural Science Foundation of China and Ministry of Science and Technology. In recent years, he has authored or coauthored more than 40 peer-reviewed scientific papers. His research interests include synthetic aperture radar interferometry as well as remote sensing classification and change detection.

Jie Dong received the B.Eng. degree in surveying and mapping engineering from the China University of Mining and Technology, Xuzhou, China, in 2011, the M.A. degree in geodesy and survey engineering from Hohai University, Nanjing, China, in 2014, and the Ph.D. degree in photogrammetry and remote sensing from the State Key Laboratory of Information Engineering in Surveying, Mapping and Remote Sensing, Wuhan University, Wuhan, China, in 2018.

Since 2018, he has been with the School of Remote Sensing and Information Engineering, Wuhan University. His current research interests include multitemporal interferometric synthetic aperture radar algorithms and geological disaster monitoring.

Juan M. Lopez-Sanchez (Senior_Member, IEEE) was born in Alicante, Spain, in 1972. He received the Ingeniero (M.S.) and Doctor Ingeniero (Ph.D.) degrees in telecommunication engineering from the Technical University of Valencia, Valencia, Spain, in 1996 and 2000, respectively.

From 1998 to 1999, he was a Predoctoral Grantholder with the Space Applications Institute, Joint Research Centre of the European Commission, Ispra, Italy. Since 2000, he has been with the Signals, Systems and Telecommunication Group, University of Alicante, Alicante, where he has been a Full Professor since 2011. He has coauthored more than 100 papers in refereed journals and more than 140 papers and presentations in international conferences and symposia. His main research interests include microwave remote sensing for inversion of biophysical parameters, polarimetric and interferometric techniques, and applications of radar remote sensing in agriculture and geophysics.
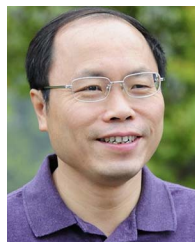
Dr. Lopez-Sanchez received the Indra Award for the best Ph.D. thesis about radar in Spain in 2001. From 2006 to 2012, he was the Chair of the Spanish Chapter of the IEEE Geoscience and Remote Sensing Society.

Yian Wang received the B.S. degree in surveying and mapping engineering from the Anhui University of Science and Technology, Huainan, China, in 2016, and the M.S. degree in geodesy and surveying engineering from Hohai University, Nanjing, China, in 2019. He is currently working toward the Ph.D. degree in signal theory and communications from the Polytechnic University of Catalonia, Barcelona, Spain and photogrammetry and remote sensing from Wuhan University, Wuhan, China, and also with the Department of Signal Theory and Communications, Polytechnic University of Catalonia.

His current research interests include SAR image denoising, multitemporal interferometric SAR algorithms, and geological disaster monitoring.

Hao Feng received the B.S. degree in geographic information system from the Nanjing University of Posts and Telecommunications, Nanjing, China, in 2014, and the M.Eng. degree in surveying and mapping engineering in 2016 from Wuhan University, Wuhan, China, where he is currently working toward the Ph.D. degree in photogrammetry and remote sensing with the State Key Laboratory of Information Engineering in Surveying, Mapping and Remote Sensing.

His research interests include multitemporal synthetic aperture radar image processing and change detection.

Mingsheng Liao received the B.S. degree in electronic engineering from the Wuhan Technical University of Surveying and Mapping (WTUSM), Wuhan, China, in 1982, the M.A. degree in electronic and information engineering from the Huazhong University of Science and Technology, Wuhan, in 1985, and the Ph.D. degree in photogrammetry and remote sensing from WTUSM in 2000.

He has been a Professor with the State Key Laboratory of Information Engineering in Surveying, Mapping and Remote Sensing, Wuhan University, Wuhan, since 1997. He is the Principal Investigator of several projects funded by the Ministry of Science and Technology (MOST), China, and the National Natural Science Foundation of China. He is also the Co-Principal Investigator of the ESA-MOST Cooperative Dragon I project from 2004 to 2008, II project from 2008 to 2012, III project from 2012 to 2016, and IV project from 2016 to 2020. He has authored or coauthored more than 60 peer-reviewed journal papers and several book chapters focused on synthetic aperture radar interferometry techniques and applications. His research interests include remote sensing image processing and analysis, algorithms for interferometric synthetic aperture radar, integration and fusion of multisource spatial information, and applications of remote sensing data.